Available online at www.sciencedirect.com
SCIENCE DIRECT®
Combustion and Flame 142 (2005) 1–16
Combustion and Flame
www.elsevier.com/locate/combustflame

Shapes of nonbuoyant round hydrocarbon-fueled laminar-jet diffusion flames in still air

C. Aalburg [a], F.J. Diez [a], G.M. Faeth [a,✠], P.B. Sunderland [b], D.L. Urban [c,*], Z.-G. Yuan [c]

[a] *The University of Michigan, Ann Arbor, MI 48109, USA*
[b] *The University of Maryland, College Park, MD 20742, USA*
[c] *NASA Glenn Research Center, Mail Stop 77-5, 21000 Brookpark Road, Cleveland, OH 44135, USA*

Received 26 January 2004; received in revised form 7 December 2004; accepted 27 December 2004

Available online 1 February 2005

Abstract

The soot-luminosity boundaries (near the laminar smoke-point condition) of steady nonbuoyant round hydrocarbon/air laminar-jet diffusion flames at microgravity were found from color video images obtained on orbit during three flights of the Space Shuttle Columbia (flights STS-83, STS-94, and STS-107); these test conditions included ethylene- and propane-fueled flames burning in still air at an ambient temperature of 300 K, ambient pressures of 35–130 kPa, jet exit diameters of 0.40–2.70 mm, and jet exit Reynolds numbers of 46–1186 to yield steady round flames, with most of the flames near the laminar smoke-point condition (including flames both emitting and not emitting soot). These results were supplemented by observations of the flame-sheet locations (locations where the local mixture fraction is stoichiometric) of nonbuoyant round soot-free and soot-containing hydrocarbon/air laminar-jet diffusion flames at microgravity found from filtered color images (at the CH line or 430 ± 5 nm) obtained using a 2.2-s free-fall facility; these test conditions included methane-, ethane-, and propane-fueled flames burning in still air at an ambient temperature of 300 K, ambient pressures of 25–98 kPa, jet exit diameters of 0.42–3.25 mm, and jet exit Reynolds numbers of 10–625. Simplified expressions to estimate soot-luminosity boundaries (near the laminar smoke-point condition) and flame-sheet locations were obtained using the classic analysis of D.B. Spalding (Combustion and Mass Transfer, Pergamon, New York, 1979, p. 185), extended empirically to account for the presence of soot luminosity for flames near the laminar smoke-point condition. The extended Spalding analysis provided good correlations of both soot-luminosity boundaries (near the laminar smoke-point condition) and flame-sheet locations for flames having short characteristic residence times where radiative heat losses from the flames were small. These results showed that soot-luminosity lengths near the laminar smoke-point condition were roughly twice as long as the flame-sheet location for both soot-free (blue) and soot-containing flames under comparable conditions due to the presence of luminous soot particles beyond the flame sheet within the fuel-lean portion of the flames.

* Corresponding author. Fax: +1 216 433 8050.
E-mail address: david.urban@grc.nasa.gov (D.L. Urban).
✠ The remaining authors regret to report that their coauthor, colleague and advisor Prof. G.M. Faeth passed away unexpectedly on January 24, 2005, after the present paper had been accepted for publication.

0010-2180/$ – see front matter
doi:10.1016/j.combustflame.2004.12.009

Keywords: Laminar diffusion flames; Nonbuoyant flames; Soot-containing flames; Flame shapes; Flame structure; Microgravity

1. Introduction

Observations of steady, nonbuoyant round hydrocarbon-fueled laminar-jet nonpremixed (diffusion) flames burning in still air are described, considering both soot-containing and soot-free (blue) flames. Steady laminar diffusion flames are of interest because they provide model flame systems that are far more tractable for theoretical and experimental studies than are more practical but unsteady and flickering turbulent diffusion flames. Steady laminar diffusion flames also merit study because understanding their structure clearly is a necessary precursor to understanding the structure of more complex unsteady turbulent diffusion flames. In addition, many aspects of steady laminar diffusion flames are relevant to unsteady turbulent diffusion flames by application of the widely recognized laminar flamelet concept of turbulent diffusion flames of Bilger [1]. The present investigation specifically considered the shapes of steady laminar diffusion flames, which is a property that has attracted numerous investigations since the classic study of Burke and Schumann [2]. This interest follows because simple nonintrusive measurements yield flame shapes that can be used to evaluate predictions of laminar flame structure. A concern about measurements of the shapes of steady laminar diffusion flames at normal gravity, however, involves the intrusion of disturbances due to buoyancy caused by Earth's gravity, because such disturbances are not relevant to practical diffusion flames that usually have relatively large flow velocities and are little affected by buoyancy [3]. Thus, the present investigation sought measurements of the shapes of classic steady, nonbuoyant round hydrocarbon-fueled laminar-jet diffusion flames burning in still air by exploiting the microgravity environments of both a flight-based orbiting space shuttle facility and a ground-based free-fall facility and subsequently using these measurements to evaluate a simplified analysis of the shapes of these flames. In particular, the present study extended earlier work along these lines by Urban et al. [4], Lin et al. [5], and Sunderland et al. [6] that involved measurement difficulties due to effects of excessive radiative heat losses and uncertainties about the transient development of the test flames.

Earlier studies of the shapes of steady, nonbuoyant round hydrocarbon-fueled laminar-jet diffusion flames have been reviewed by Urban et al. [4] and Lin et al. [5]; therefore, the present discussion of past work is brief. Initial experimental studies of these flames were undertaken by Cochran and coworkers [7–9] and Edelman and co-workers [10–12]. There were two concerns about these observations, however, as follows: (1) potential effects of transient flame development for the limited test times of ground-based low-gravity facilities used to obtain nonbuoyant flames were difficult to assess, and (2) the luminous shapes of these hydrocarbon-fueled flames were due largely to the presence of glowing soot particles, which are known to be present beyond the flame sheet where the local mixture fraction is stoichiometric (which was a concern because the flame sheet was the flame-shape condition used in early theories), particularly as the laminar smoke-point condition (the first condition where the flame begins to emit soot as defined by Schug et al. [13]) is approached, see Refs. [14–19].

Later studies of steady, nonbuoyant round hydrocarbon-fueled laminar-jet diffusion flames by Sunderland et al. [20], Urban et al. [4], and Lin et al. [5] sought to rectify the limitations of earlier work. Sunderland et al. [20] emphasized flame-sheet properties using a CH line filter (430 ± 5 nm) to block soot luminosity so that the flame sheet could be observed, and sought to reduce effects of transient flame development by observing flames at low pressures where characteristic residence times are small which tends to minimize transient effects. Measured flame-sheet lengths and diameters were compared with predictions of the simplified analyses of Klajn and Oppenheim [21], Mahalingam et al. [22], and Roper [23], finding that although all three approaches yielded good predictions of flame lengths, only the approach of Klajn and Oppenheim [21] yielded good predictions of maximum flame diameters.

Urban et al. [4] and Lin et al. [5] measured soot-luminosity boundaries near the laminar smoke-point conditions based on measurements obtained under long-duration microgravity conditions provided by the orbiting Space Shuttle Columbia (flights STS-83 and STS-94). Flame shape measurements were compared with predictions based on the simplified analysis of Spalding [24], described in more detail by Kuo [25]. These predictions were promising using an empirical approach to treat soot-luminosity lengths; however, these flames had large characteristic residence times so that radiative heat losses from them were significant. This caused radiative quenching near the flame tips, and tip-opening phenomena prevented a thorough evaluation of the flame-shape

Nomenclature

AR	flame aspect ratio, L_f/w_{max}
C_f	empirical flame length parameter
C_w	empirical maximum flame width parameter
d	jet exit diameter
D	mass diffusivity
L_o	distance from jet exit to virtual origin
L_f	distance from jet exit to the tip of either the soot-luminosity boundary (near the laminar smoke-point condition) or the flame-sheet location
$\dot{m}$	fuel mass flow rate from burner
p	pressure
Re	flame Reynolds number, $4\dot{m}/(\pi d\mu)$
Re_o	jet exit Reynolds number, $4\dot{m}/(\pi d\mu_o)$
r	radial distance
Sc	flame Schmidt number, ν/D
t_{ch}	characteristic residence time, Eq. (1)
u_o	mean burner exit velocity, $4\dot{m}/(\pi\rho_o d^2)$
w	luminous flame diameter
w_{max}	maximum luminous flame diameter
Z_{st}	stoichiometric mixture fraction
z	streamwise distance
ζ	normalized streamwise distance, Eq. (7)
μ	dynamic viscosity
ν	kinematic viscosity
ρ	density
Subscript	
o	burner exit condition

predictions of the simplified Spalding [24] approach, in which effects of flame radiation were ignored.

Based on the previous discussion, the objectives of the present investigation were to undertake additional evaluation of the simplified flame-shape analysis of Spalding [24], considering laminar flame lengths, maximum flame diameters and luminous flame shapes for various burner diameters, burner flow rates, pressures, and hydrocarbon fuels for flames involving different degrees of soot content between the laminar soot- and smoke-point conditions. This evaluation was based on new measurements of flame-sheet boundaries for both soot-free and soot-containing flames and soot-luminosity boundaries (near the laminar smoke-point condition) carried out on the orbiting Space Shuttle Columbia (flight STS-107), emphasizing short characteristic residence times to avoid problems of quenching and tip opening due to excessive radiative heat losses. In addition, predictions of flame-sheet locations were compared with measurements from the free-fall experiments of Sunderland et al. [20] extending these results from consideration of flame-sheet lengths and maximum flame-sheet diameters to consideration of complete flame-sheet shapes.

2. Experimental methods

2.1. Flight experiments

Experimental methods for both the flight- and ground-based tests are briefly described. The flight test arrangement was nearly identical to that used during the earlier nonbuoyant round laminar-jet diffusion flame flight experiments of Urban et al. [4] and Lin et al. [5]; a sketch of this arrangement appears in Fig. 1. Laminar-jet diffusion flames were stabilized at the exit of a round fuel nozzle located along the axis of a windowed cylindrical chamber. The chamber had a diameter of 400 mm, a maximum length of 740 mm, and an internal volume of 0.082 m^3, and was operated at pressures of 35–130 kPa. The chamber was filled with oxygen/nitrogen mixtures to provide the nominal composition of dry air ($21 \pm 1\%$ oxygen by volume). The pressure, temperature, and composition of the gas surrounding the test flames all varied somewhat during flame burning periods due to the limited amount of air within the closed test chamber. The greatest change involved the composition of the gas within the chamber; however, even this property was controlled so that the maximum oxygen consumption generally did not exceed 2% by volume during the experiments. One exception was test 04E107 (for Space Shuttle flight STS-107), involving an ethylene/air flame at a total pressure of 49 kPa that had an unusually large fuel flow rate that yielded a correspondingly long flame (up to 140 mm long) where the maximum oxygen consumption reached 4.0%. The initial composition of the air within the test chamber was maintained at 21% oxygen by volume by venting the test chamber to space and adding fresh dry air prior to each test.

Over the entire test series, four fuel nozzles consisting of constant diameter cylindrical stainless-steel tubes having inside diameters of 0.40, 0.80, 1.60, and 2.70 mm and lengths of 148 mm from the inlet plenum were used. The inlets of the nozzles had flow straighteners to prevent swirl, whereas the overall length-to-diameter ratios of the passages were greater than 55:1, which was sufficient to yield fully developed laminar pipe flow at the nozzle exit ($46 \leqslant$

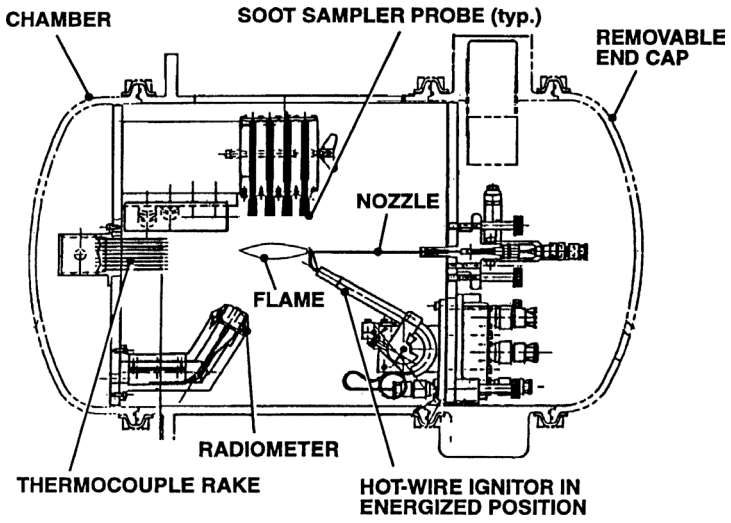

Fig. 1. Laminar soot process (LSP) apparatus for flight experiments considering steady nonbuoyant round laminar-jet diffusion flames in still air at microgravity conditions.

$Re_o \leqslant 1186$). The test fuels were stored in cylinders and were delivered to the nozzles through a solenoid valve, a mass flow rate controller and a flow limiting orifice. The flames were ignited by a hot wire coil that was retracted from the nozzle exit once ignition was complete.

Flame operation was monitored by making the following measurements: fuel flow rate with an accuracy of 0.8%, fuel temperatures at the nozzle inlet with an accuracy of ± 1.5 K, chamber pressures with an accuracy of 1.2%, and chamber gas temperatures (far from the flames) with an accuracy of ± 1 K. These measurements were recorded at a frequency of roughly 1 Hz.

Soot-luminosity boundaries and flame-sheet locations were measured from images obtained using color CCD video cameras (Hitachi Model KP-0553 during flights STS-83 and STS-94, and Panasonic Model WV-CD612 during flight STS-107). The cameras had a 125×164-mm field of view and a depth of field of 25 mm centered on the flame axis. The spatial resolution of recorded images was better than 0.3 mm. It was not possible to adjust image brightness on orbit during flights STS-83 and STS-94; therefore, camera settings were selected so that flames having the smallest levels of luminosity (based on free-fall tests) could be observed which implied that flame images generally were overexposed (although reasonably sharp images of luminous flame boundaries were still obtained). In contrast, the camera used during flight STS-107 had automatic iris and gain controls that yielded uniform maximum brightness levels for all these tests. Flame images were recorded at 30 images/s. Measured luminous flame lengths and diameters have estimated experimental uncertainties (95% confidence) less than 10%.

2.2. Ground-based experiments

The test arrangement used by Sunderland et al. [20] provided information about the flame-sheet shapes of nonbuoyant round soot-free and soot-containing laminar-jet diffusion flames burning in still air. As noted earlier, a CH line (at 430 ± 5 nm) filter was used to obtain images of the flame sheet in the presence of soot luminosity for soot-containing flames. This test arrangement was similar to the flight test apparatus. A major difference, however, was that operation at microgravity was not continuous, similar to the flight tests, but was limited to the 2.2-s duration of the free-fall facility at the NASA Glenn Research Center. In this case the laminar-jet diffusion flames were also stabilized at the exit of round fuel nozzles located along the axis of a windowed cylindrical chamber. The chamber had a diameter of 250 mm, maximum length of 530 mm, and internal volume of 0.027 m^3, and was operated at pressures of 25–98 kPa. Ambient air was used as the environment for all the experimental results considered here. Test operating periods were short for these experiments; therefore, the pressure, temperature, and composition of the air surrounding the test flames varied to a negligible degree. The test chamber was evacuated and filled with fresh ambient air prior to each test.

Over the entire test series, four fuel nozzles consisting of 222-mm stainless-steel tubes having inside diameters of 0.42, 0.85, 1.70, and 3.25 mm, were used. There was no evidence of swirl flow at the nozzle exit, whereas the overall length to diameter ratios of the nozzle passages were greater than 68:1, which was sufficient to yield fully developed laminar pipe flow at the nozzle exit ($10 \leqslant Re_o \leqslant 625$). The test fu-

els were stored in a cylinder and were delivered to the nozzle via a pressure regulator, a solenoid valve, a critical-flow orifice, a mass flow rate sensor, and a second solenoid valve. The flames were ignited after release into the microgravity environment using a retractable hot wire ignitor.

The present measurements were extended from the flame-sheet lengths and maximum flame-sheet diameters found by Sunderland et al. [20] to flame-sheet shapes. Flame-sheet shapes were observed using a color CCD camera (Panasonic WV-CL352). Flame luminosity variations were handled by varying the focal lengths (16–50 mm) and f numbers (1.4–6.0) of the camera lens. Spatial resolution was 0.1 mm or better. Measured flame sheet lengths and diameters have estimated experimental uncertainties (95% confidence) less than 5%.

2.3. Test conditions

The potential of the flames to have excessive radiative heat losses can be estimated from their characteristic residence times, t_{ch}, taken to be the time for the flow to convect from the burner exit to either the soot-luminosity boundary or the flame-sheet location, as follows:

$$t_{ch} = 2L_f/u_o. \quad (1)$$

In deriving this relationship, the average velocity for this convection process in a nonbuoyant flame was taken to be $u_o/2$ because streamwise velocities along the axis of nonbuoyant laminar-jet diffusion flames decrease rather rapidly.

The test conditions of the flight-based microgravity experiments are summarized in Table 1. The results obtained during flights STS-83 and STS-94 involved flames near the laminar smoke-point condition; in addition, test flames 01E083 and 03E083 of flight STS-83 and 01E094 and 10P094 of flight STS-94 had open tips and were actually soot emitting. During the tests of flights STS-83 and STS-94, all but test 03E083 of flight STS-83 and tests 03E094 and 17E094 of flight STS-94 involved flames that had relatively large characteristic residence times and excessive radiative heat losses that resulted in quenching of the flame near its tip, yielding open-tipped flames. In contrast, flame residence times were reduced for the flames considered during flight STS-107, and all these flames involved relatively small radiative heat losses and had closed tips.

The ground-based test conditions are summarized in Table 2. In this case all the flames yielded flame sheet locations and had closed-tip flame-sheets, with roughly half being soot-free flames and the other half being soot-containing flames. Unfortunately, many of these flames had aspect ratios (ARs) <3, and were not good candidates to evaluate the simplified Spalding [24] flame-shape analysis which involved the assumption of relatively large aspect ratio flames satisfying the boundary-layer approximations.

3. Theoretical methods

The objective of the analysis of flame shapes was to develop a convenient way to interpret and correlate measurements of soot-luminosity boundaries (near the laminar smoke-point condition) and flame-sheet locations. Thus, a set of easily used equations was sought, combined with recommendations for selecting thermochemical and transport properties appearing in these equations to obtain good estimates of flame-shape properties, rather than a detailed formulation that would require numerical solutions on a computer. This was done based on the simplified analysis of the structure of nonbuoyant round laminar-jet diffusion flames due to Spalding [24]. In the following description of this analysis, the nozzle exit fluid is assumed to contain the fuel and the ambient fluid is assumed to contain the oxidant because this corresponds to the configuration of the flames used to evaluate the predictions (i.e., so-called inverse diffusion flames are not considered); in addition, this is the conventional configuration used to determine laminar soot- and smoke-point conditions which are useful properties for defining the degree to which diffusion flames contain soot. The following description of the analysis is brief; see Spalding [24], Kuo [25], and Lin et al. [5] for more details.

Major assumptions of the flame-shape analysis of Spalding [24] are as follows: (1) steady round laminar-jet diffusion flames are burning at constant pressure in a still environment; (2) effects of buoyancy and associated changes in potential energy are negligible; (3) the Mach number of the flow is small so that effects of viscous dissipation and changes in kinetic energy can be ignored; (4) the flames have a large aspect ratio so that effects of diffusion of mass (species) and momentum in the streamwise direction are small and the boundary layer approximations apply; (5) for the same reasons, the solution of the governing equations can be approximated by far-field conditions where the details of the initial conditions at the jet exit can be replaced by jet invariants representing conservation of mass (elements) and momentum in the flow, in the integral sense; (6) all chemical reactions are fast and occur within a thin flame sheet so that fuel and oxidant are never simultaneously present at finite concentrations; (7) the diffusivities of mass (of all species) are equal, and the ratios of mass and momentum diffusivities are represented by a constant Schmidt number; (8) all thermophysical and transport

Table 1
Summary of flight-based tests[a]

Test	Type[b]	d (mm)	p (kPa)	$\dot{m}$ (mg/s)	u_o[c] (mm/s)	Re_o[d]	t_{ch} (ms)	L_f (mm)	w_{max} (mm)	AR
Flight STS-83, C_2H_4/air flames, $Z_{st} = 0.0636$										
01E083	OT/SE	1.60	100	1.84	820	138	121	49.3	13.7	3.6
03E083	CT/SE	1.60	50	1.84	1630	138	77	63.0	14.2	4.4
Flight STS-94, C_2H_4/air flames, $Z_{st} = 0.0636$										
01E094	OT/SE	1.60	100	0.71	320	54	130	20.6	12.6	1.6
02E094	CT/SP	1.60	50	0.76	670	57	53	17.7	13.1	1.4
03E094	CT/SP	1.60	50	1.29	1140	97	64	36.5	13.8	2.6
04E094	OT/SP	1.60	65	0.91	620	68	86	26.5	13.1	2.0
14E094	OT/SP	1.60	80	0.67	370	50	97	18.0	12.9	1.4
15E094	OT/SP	1.60	100	0.61	270	46	109	14.7	11.5	1.3
16E094	CT/SP	1.60	65	0.74	510	56	75	19.0	13.4	1.4
17E094	CT/SP	1.60	35	1.34	1690	100	40	34.0	14.7	2.3
05E094	OT/SP	2.70	65	1.14	270	51	215	29.1	21.4	1.4
06E094	OT/SP	2.70	80	1.16	230	51	269	30.3	20.9	1.4
07E094	OT/SP	2.70	100	1.08	170	48	302	25.5	19.6	1.3
08E094	OT/SP	2.70	50	1.38	430	62	173	37.3	21.4	1.7
Flight STS-94, C_3H_8/air flames, $Z_{st} = 0.0602$										
09P094	OT/SP	1.60	130	0.78	170	73	277	23.3	17.4	1.3
10P094	OT/SE	1.60	50	1.82	1020	172	120	61.4	18.8	3.3
11P094	OT/SP	1.60	65	1.22	530	116	144	38.1	17.4	2.2
12P094	OT/SP	1.60	100	0.88	250	83	218	27.1	16.6	1.6
13P094	OT/SP	1.60	80	1.04	370	99	177	32.4	17.2	1.9
18P094	CT/SP	1.60	80	0.82	290	78	164	23.9	16.9	1.4
19P094	OT/SP	1.60	100	0.71	200	67	191	19.0	16.1	1.2
Flight STS-107, C_2H_4/air flames, $Z_{st} = 0.0636$										
41E107	CT/SC	0.80	100	0.65	1120	98	27.6	17.1	6.5	2.6
02E107	CT/SP	0.80	100	1.46	2520	219	23.0	32.1	5.2	6.2
04E107*	CT/SF	0.80	49	2.00	7060	299	8.6	34.2	5.7	6.0
04E107	CT/SP	0.80	49	3.96	13,980	595	14.3	110.2	10.1	10.9
05E107	CT/SC	0.80	48	1.99	7170	299	9.8	38.6	6.0	6.4
51E107	CT/SC	0.40	98	3.95	27,880	1186	5.3	81.1	4.9	16.6
52E107	CT/SC	0.40	99	1.51	10,550	453	6.2	35.9	3.8	9.4
Flight STS-107, C_3H_8/air flames, $Z_{st} = 0.0602$										
53E107	CT/SF	0.40	47	1.71	25,170	513	2.5	32.6	4.1	8.0
46P107	CT/SC	0.80	99	0.53	590	100	52.2	15.8	11.2	1.4
07P107	CT/SC	0.80	48	0.99	2270	188	22.4	26.1	7.9	3.3
08P107	CT/SP	0.80	100	1.21	1330	229	47.0	32.1	7.9	4.1
54P107	CT/SP	0.40	99	1.77	7870	671	12.4	50.0	5.4	9.3
55P107	CT/SP	0.40	99	1.77	7870	671	12.9	52.0	6.0	8.7

[a] Meaurements of Urban et al. [4] during STS-83, measurements of Lin et al. [5] during STS-94, and present measurements during STS-107.

[b] Type: CT, closed tip; OT, open tip; SP, laminar smoke point; SE, soot emitting; SC, soot containing (between soot and smoke points); SF, soot free.

[c] Mean velocity based on fuel density at jet exit (nominal pressure and 300 K).

[d] Mean Reynolds number based on fuel viscosities at jet exit (300 K), i.e., 10.6 mg/(ms) for ethylene and 8.4 mg/(ms) for propane.

properties are assumed to be constant throughout the flame; and (9) effects of radiative and other heat losses are small. See Lin et al. [5] for a justification of these approximations.

Based on the approximations that were just summarized, the expression for either the soot-luminosity or flame-sheet length, L_f, becomes [5]

$$(L_f - L_o)/d = 3C_f ReSc/(32Z_{st}), \quad (2)$$

where L_o is a virtual origin used to extend the range of conditions under which Eq. (2) is useful, d is the burner diameter, C_f is an empirical coefficient having a value on the order of unity that is used to treat the effect of soot luminosity on the flame length, Re is the

Table 2
Summary of ground-based tests[a]

Test	Type[b]	d (mm)	p (kPa)	$\dot{m}$ (mg/s)	u_o[c] (mm/s)	Re_o[d]	t_{ch} (ms)	L_f (mm)	w_{max} (mm)	AR
CH_4/air flames, $Z_{st} = 0.0551$										
01M	CT/SC	0.42	98	1.70	19,270	470	3.4	32.4	5.6	5.8
02M	CT/SC	0.42	98	2.27	25,640	625	3.2	41.0	5.3	7.7
03M	CT/SC	0.85	50	0.90	4950	123	8.0	19.8	9.9	2.0
04M	CT/SC	0.85	98	0.89	2450	121	15.1	18.5	9.3	2.0
05M	CT/SC	0.85	98	1.69	4650	230	13.8	32.1	9.7	3.3
06M	CT/SF	0.85	98	0.42	1150	57	19.0	10.9	9.1	1.2
07M	CT/SC	1.70	25	0.86	2360	58	19.9	23.4	22.6	1.0
08M	CT/SF	1.70	25	0.42	1150	28	16.2	9.3	13.9	0.7
09M	CT/SF	1.70	50	0.42	570	28	39.5	11.3	15.2	0.7
10M	CT/SC	1.70	50	0.86	1180	58	41.7	24.5	20.1	1.2
11M	CT/SC	1.70	50	0.86	1180	59	46.5	27.4	23.4	1.2
12M	CT/SC	1.70	98	0.42	290	28	69.9	10.0	12.5	0.8
13M	CT/SC	1.70	98	0.86	590	58	89.0	26.2	19.9	1.3
14M	CT/SF	3.25	98	0.42	80	15	239	9.4	13.2	0.7
15M	CT/SF	3.25	98	0.51	100	18	227	10.8	15.8	0.7
C_2H_6/air flames, $Z_{st} = 0.0588$										
16EA	CT/SF	0.42	50	0.88	10,660	294	3.0	15.8	5.1	3.1
17EA	CT/SF	0.85	25	0.13	740	21	7.7	2.8	4.6	0.6
18EA	CT/SF	0.85	25	1.02	5960	165	7.9	23.9	12.2	2.0
19EA	CT/SF	0.85	50	0.14	400	22	12.3	2.5	4.1	0.6
20EA	CT/SC	0.85	50	2.06	6010	333	15.1	45.4	12.4	3.7
21EA	CT/SF	1.70	50	1.02	740	83	68.6	25.5	21.0	1.2
22EA	CT/SF	1.70	98	0.50	180	41	112.1	10.2	12.9	0.8
23EA	CT/SF	3.25	25	0.55	220	23	96.9	10.7	16.7	0.6
24EA	CT/SF	3.25	50	0.24	50	10	193	4.6	8.3	0.6
25EA	CT/SF	3.25	50	1.06	210	45	201	21.3	26.3	0.8
26EA	CT/SF	3.25	98	0.24	20	10	385	4.6	7.9	0.6
27EA	CT/SF	3.25	98	0.50	50	21	379	9.5	14.2	0.7
C_3H_8/air flames, $Z_{st} = 0.0602$										
28P	CT/SC	0.85	25	1.70	6780	312	10.6	36.0	14.2	2.5
29P	CT/SC	0.85	25	2.18	8680	400	11.0	47.8	15.6	3.1
30P	CT/SC	1.70	98	0.52	130	47	158	10.2	13.5	0.8
31P	CT/SC	1.70	98	1.02	260	94	172	22.0	21.1	1.0
32P	CT/SC	1.70	98	1.06	260	97	183	24.1	22.0	1.1
33P	CT/SC	3.25	50	1.02	140	49	262	18.3	27.2	0.7
34P	CT/SC	3.25	98	0.51	30	24	429	7.4	12.7	0.6
35P	CT/SC	3.25	98	1.02	70	49	378	13.2	18.2	0.7
36P	CT/SC	3.25	98	1.02	70	49	542	19.0	22.7	0.8

[a] Meaurements of Sunderland et al. [20].
[b] Type: CT, closed tip; OT, open tip; SP, laminar smoke point; SE, soot emitting; SC, soot containing (between soot and smoke points); SF, soot free.
[c] Mean velocity based on fuel density at jet exit (nominal pressure and 300 K).
[d] Mean Reynolds number based on fuel viscosities at jet exit (300 K), i.e., 12.7 mg/(ms) for methane, 10.6 mg/(ms) for ethane, and 8.4 mg/(ms) for propane.

flame Reynolds number, Sc is the flame Schmidt number (taken to have a constant value of 0.76 for present results), and Z_{st} is the stoichiometric mixture fraction (taken to be the mass fraction of the burner exit fluid when combined with the ambient fluid so that the concentrations of fuel and oxidant in the mixture are present in stoichiometric proportions; see Tables 1 and 2 for the values of Z_{st} for the present flames).

Noting that the expression used to find Re is based on the burner mass flow rate, Eq. (2) can be rearranged to yield

$$L_f - L_o = 3C_f \dot{m} Sc/(8\pi\mu Z_{st}), \tag{3}$$

where $\dot{m}$ is the burner mass flow rate (which was the fuel mass flow rate for present test conditions), and μ is the dynamic viscosity, taken to have the value for

air at the average temperature of the flame from Braun et al. [26] because nitrogen dominates the composition of the flame gases when hydrocarbons are burned in air. The maximum flame diameter, $w_{\max}$, is given by the expression

$$w_{\max} Z_{\mathrm{st}}/d = C_{\mathrm{w}}, \tag{4}$$

where the value of C_{w} from the Spalding [24] theory is

$$C_{\mathrm{w}} = 9/16 \quad \text{at } (z - L_{\mathrm{o}})/(L_{\mathrm{f}} - L_{\mathrm{o}}) = 9/16, \tag{5}$$

where z is the streamwise distance from the burner exit, and in this case there was no effect of soot content in the flame on the value of $w_{\max}$. Finally, the flame shape, i.e., the luminous flame diameter, w, as a function of streamwise distance from the burner exit, is given by

$$w Z_{\mathrm{st}}/d = 3^{1/2} \zeta \left(\zeta^{-1/2} - 1\right)^{1/2}, \tag{6}$$

where

$$\zeta = (z - L_{\mathrm{o}})/(L_{\mathrm{f}} - L_{\mathrm{o}}). \tag{7}$$

Although flame-length properties are affected by the assumed transport properties of the flow and the presence of soot, as indicated by Eq. (2), flame-diameter properties, and thus the flame shape, are only indirectly affected by assumed transport properties and the presence of soot through the computation of flame length, based on Eqs. (2)–(7).

4. Results and discussion

4.1. Flame development

The general nature of the space-based test flames observed during the earlier experiments carried out during Space Shuttle Columbia flights STS-83 and STS-94 is discussed by Urban et al. [4] and Lin et al. [5]. The typical operation of the present space-based test flames during flight STS-107 can be seen from the plot of the monitoring measurements during tests 04E107 and 04E107* involving an ethylene/air flame, having a burner diameter of 0.8 mm and a pressure of 49 kPa, illustrated in Fig. 2. The following flame properties are shown as a function of time after ignition: ignitor and soot sampler timing, fuel flow rate, ambient oxygen concentration (calculated assuming stoichiometric combustion of the total mass of fuel injected up to a given time), luminous flame length, maximum luminous flame diameter, plume temperature at the flame axis, radiant heat flux, ambient chamber temperature, and ambient chamber pressure. Ignitor timing refers to hardware actuation when the ignitor heater coil is positioned near the exit of the

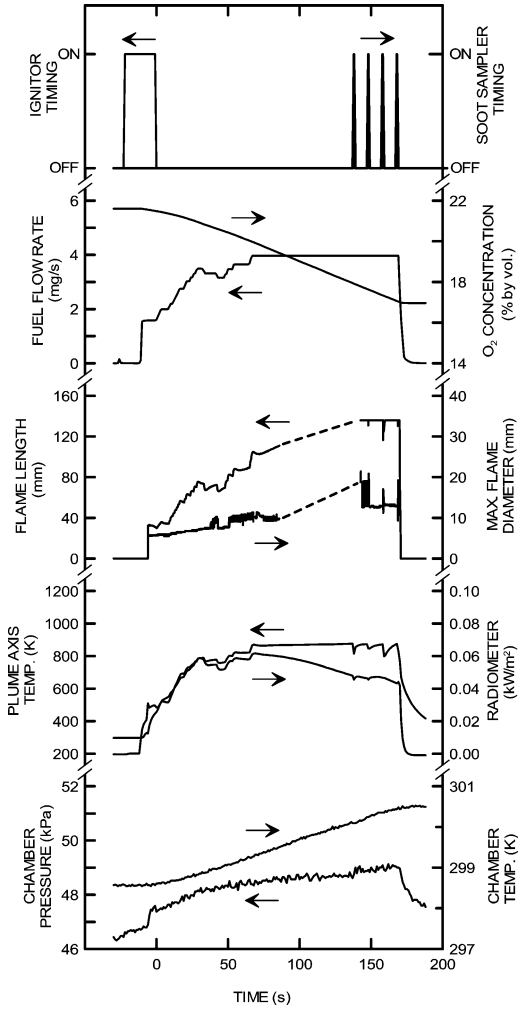

Fig. 2. Monitoring measurements as a function of time for a typical flame during a flight experiment: ignitor and soot sampler timing, fuel flow rate, ambient oxygen concentration, luminous flame length, maximum luminous flame diameter, plume axis temperature, radiometer output, chamber pressure and chamber temperature. Complete record of monitoring measurements for tests 04E107* and 04E107 for an ethylene/air flame at 49 kPa for the 0.8-mm-diameter burner.

burner nozzle and then removed; soot sampler spikes indicate insertion and retraction of four soot samplers into the test flame. During this test, the aim was to initially view flames under near-soot-free (blue) conditions to observe flame-sheet properties; this condition is denoted as test 04E107* in Table 1. Thus, after ignition for tests 04E107* and 04E107, the fuel flow rate was maintained constant until the soot-free (blue) flame condition was approached, providing results denoted as test 04E107*; then the fuel flow rate was gradually increased until laminar smoke-point conditions were approached, providing results denoted as

test 04E107. The latter condition produced a rather large aspect ratio flame having a length of 110.2 mm. One difficulty with the test illustrated in Fig. 2, however, is that video observations of the flame were interrupted in the period when imaging data for soot concentration and temperature distributions were obtained (this period is indicated by the dashed-line portions of the flame length and maximum flame diameter plots). The results exhibit the rather large degree of oxygen consumption mentioned earlier for this test due to the large fuel flow rate and relatively small chamber pressure.

The characteristic development time of the flame illustrated in Fig. 2 is only 14.3 ms (see Table 1), which is short compared with the time scale used in Fig. 2. This accounts for the relatively rapid adjustment of flame diameters and lengths to changes in the burner fuel flow rate seen in this figure. Plume axis temperatures reach large values mainly because the large flame length caused the tip of the flame to approach the thermocouple used for these temperature measurements. Flame radiation levels initially increase in the period when the fuel flow rate is increased and then decrease again as reduced ambient oxygen concentrations cause flame temperatures to decrease. Variations of chamber temperature and pressure are modest over the duration of the test due to the relatively large volume of the test chamber used for these experiments.

4.2. Flame lengths

Unlike earlier flight-based experiments in this series obtained during flights STS-83 and STS-94, excessive radiative heat losses, leading to quenching of the flame tip and tip-opening behavior, did not occur during the experiments of flight STS-107; instead, all these flames were steady and had closed tips. Steady, closed-tip flames were also observed during the flame-sheet location observations reported by Sunderland et al. [20], which also are considered in the following. As noted earlier, these tests involved both soot-free and soot-containing flames; however, an optical filter allowed the flame sheet to be observed even when soot was present.

Measurements and predictions of luminous flame lengths are illustrated in Fig. 3, which is plotted to demonstrate the simple relationship between luminous flame lengths and fuel flow rates through the burner suggested by Eq. (3). For these results, luminous flame lengths from tests carried out during flights STS-83 and STS-94 involved the soot-

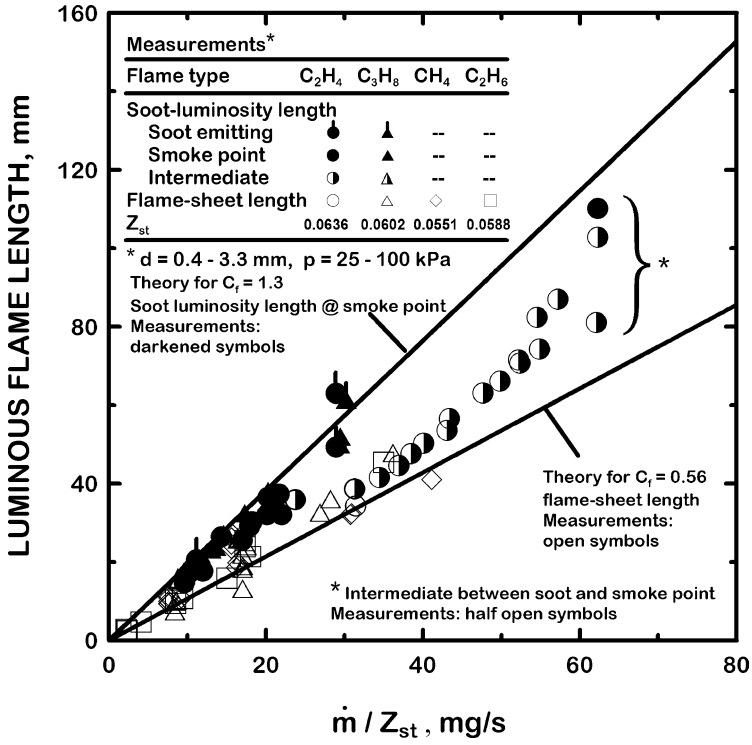

Fig. 3. Measured and predicted soot-luminosity and flame-sheet lengths of nonbuoyant hydrocarbon/air flames as a function of fuel flow rate. Measurements of Lin et al. [5], Sunderland et al. [20], and the present investigation as summarized in Tables 1 and 2; predictions based on the extended Spalding [24] approach, Eq. (3).

luminosity lengths (near laminar smoke-point conditions) and mainly were open-tip flames, although Lin et al. [5] noted that tip opening did not affect the length of the soot-luminosity boundaries to a significant degree. In Fig. 3, solid symbols denote soot-luminosity lengths (near the laminar smoke-point conditions), mainly from the flight-based experiments of Urban et al. [4], Lin et al. [5], and the present investigation. In contrast, open symbols denote flame-sheet lengths, mainly from the free-fall experiments of Sunderland et al. [20], whereas half-solid symbols denote soot-luminosity lengths under intermediate conditions for flames between laminar soot- and smoke-point conditions, mainly from the flight-based experiments of Urban et al. [4], Lin et al. [5], and the present investigation. Predictions from the simplified analysis of Spalding [24] are also illustrated on the plot, based on best-fit correlations of the measurements illustrated in Fig. 3, yielding $C_f = 1.13$ for the soot-luminosity length of soot-containing flames (near the laminar smoke-point condition) and $C_f = 0.56$ for the flame-sheet length of both soot-free and soot-containing flames. Effects of the virtual origin were not large for the results illustrated in Fig. 3; therefore, L_o/d was taken to be zero to minimize the complexity of the correlation of Eq. (3). This practice is followed throughout the present article. In view of its simplicity, it is remarkable how well the Spalding [24] analysis provides correlations of the soot-luminosity (near the laminar smoke-point condition) and flame-sheet lengths with values of C_f on the order of unity and L_o/d small, as expected. Finally, the measurements of flame test 04E107, discussed in connection with the monitoring measurements of Fig. 2, provide a nice illustration of the way that luminous soot particles in the fuel-lean region of the flames extend soot-luminosity lengths as the fuel flow rate increases from the laminar soot-point condition toward the laminar smoke-point condition. In particular, at small fuel flow rates near the start of combustion, this flame was relatively short, nearly blue, and close to the laminar flame-sheet correlation in Fig. 3, whereas toward the end of observations this flame was quite long (the longest flame illustrated in Fig. 3), and was brightly luminous, with the soot-luminosity length approaching the laminar smoke-point correlation in Fig. 3.

4.3. Flame diameters

The normalized maximum flame diameter, $w_{max}Z_{st}/d$, is simply a constant value, predicted to be equal to 9/16, according to Eqs. (4) and (5). This implies that the maximum flame diameters of nonbuoyant laminar-jet diffusion flames burning in still air are only functions of the jet exit diameter and the stoichiometric mixture fraction (the latter varying to only a relatively small degree for the present experiments based on the property values summarized in Tables 1 and 2). In addition, no particular variation of the maximum flame diameter was observed as a function of the degree of soot present in the flames; i.e., the maximum diameters of the flame-sheet location and the soot-luminosity boundary (near the laminar smoke-point condition) were essentially the same.

Measured and predicted normalized maximum flame diameters, $w_{max}Z_{st}/d$, are plotted as a function of normalized flame length, L_f/d, in Fig. 4. Measurements are illustrated for all the tests considered during the present investigation, as summarized in Tables 1 and 2. Similar to the flame-length results illustrated in Fig. 3, solid symbols denote maximum soot-luminosity diameters (near the laminar smoke-point condition), mainly from the flight experiments of Urban et al. [4], Lin et al. [5], and the present investigation; open symbols denote maximum flame-sheet diameters, mainly from the free-fall experiments of Sunderland et al. [20]; and half-solid symbols denote maximum soot-luminosity diameters under intermediate conditions for flames having lengths between soot- and smoke-point conditions, mainly from the flight experiments of Urban et al. [4], Lin et al. [5], and the present investigation. As noted earlier, L_o/d has been taken to be zero for all these results to minimize the complexity of the correlation of Eqs. (4) and (5). Finally, also as noted earlier, maximum soot-luminosity and flame-sheet diameters were little affected by the degree of soot present in the flames.

For $L_f/d < 10$ in Fig. 4, the values of $w_{max}Z_{st}/d$ progressively increase with increasing values of L_f/d and, thus, increasing values of the fuel flow rate. This behavior is not surprising, however, because flames having $L_f/d < 10$ generally have small aspect ratios, AR < 3, and are not good candidates for application of the boundary-layer approximations used to derive Eq. (4). In contrast, for $L_f/d > 10$, the measured values of $w_{max}Z_{st}/d$ are relatively independent of the flame length and yield a mean value of $C_w = 0.65$, with an uncertainty (95% confidence) of 15%, whereas the simplified analysis of Spalding [24] yields $C_w = 9/16 = 0.56$. Thus, the present measurements agree with the simplified Spalding [24] analysis within the experimental uncertainties of the measurements.

The results of Eqs. (3) and (4), plotted in Figs. 3 and 4, highlight the fact that the length of steady round nonbuoyant laminar-jet diffusion flames is proportional to the fuel mass flow rate, and is affected by the soot content of the flames, but is independent of the burner diameter and pressure for given flame reactants. On the other hand, for flames having $L_f/d > 10$, the maximum flame diameter is propor-

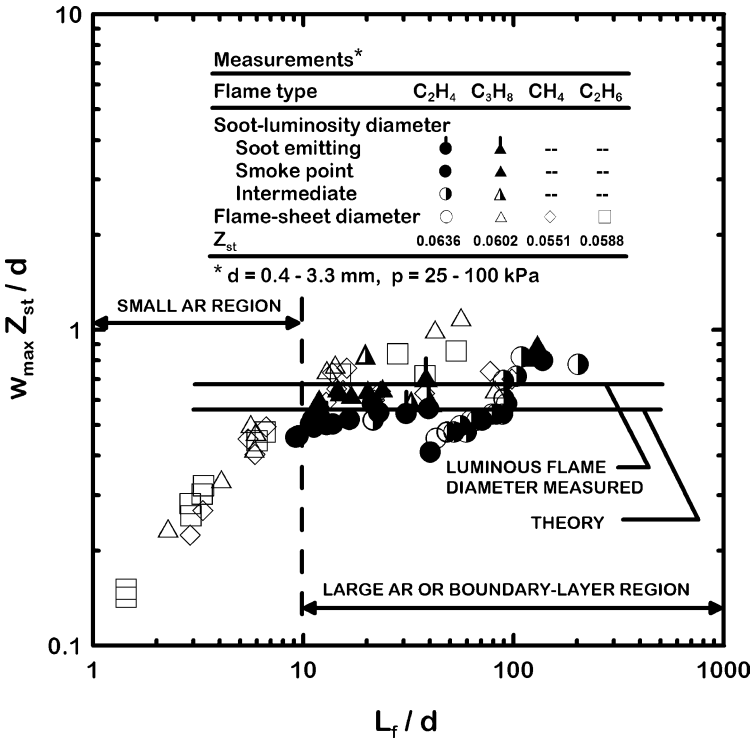

Fig. 4. Measured and predicted maximum soot-luminosity and flame-sheet diameters of nonbuoyant hydrocarbon/air flames as a function of luminous flame length. Measurements of Urban et al. [4], Lin et al. [5], Sunderland et al. [20], and the present investigation as summarized in Tables 1 and 2; predictions based on the extended Spalding [24] approach, Eq. (4).

tional to the burner diameter, and is not affected by the soot content of the flames, the burner fuel flow rate, or the pressure for given flame reactants. Thus, it is possible to create long thin pencil-like flames, satisfying the boundary-layer approximations, by using large fuel flow rates along with small burner diameters, at least for conditions not subject to flame liftoff and blowout.

4.4. Flame shapes (flight-based experiments)

The final step in the evaluation of the simple flame-shape analysis of Spalding [24] involved consideration of complete luminous flame shapes for various burner conditions and degrees of soot content of the flames. This involved comparing the predictions of Eqs. (6) and (7) with measurements of flame shapes for steady nonbuoyant round laminar-jet diffusion flames burning in still air, considering a variety of changes of flame operating conditions to test the capabilities of the extended Spalding [24] analysis. These results are described in the following considering findings from both the flight- and ground-based experiments, with the flight-based experiments considered first, in this section.

Photographs of three flames observed during the flight-based experiments (Fig. 5) show the effects of fuel flow rate and burner diameter on the shapes of ethylene-fueled flames burning in air at pressures of 49–50 kPa. The test parameters of these flames are as follows: the left flame is from test 04E107* for a burner diameter of 0.8 mm and a fuel flow rate of 2.00 mg/s to yield a flame near the laminar soot-point condition where the flame has just started to indicate the presence of soot, and the soot-luminosity boundary and the flame-sheet shape are nearly the same; the middle flame is from test 04E107 for a burner diameter of 0.8 mm and a fuel flow rate of 3.96 mg/s to yield a soot-luminosity boundary near the laminar smoke-point condition; and the right flame is from test 03E94 for a burner diameter of 1.6 mm and a fuel flow rate of 1.29 mg/s to yield a soot-luminosity boundary also near the laminar smoke-point condition. Finally, the measured and predicted (with predictions from the extended Spalding [24] analysis using the measured flame length to define values of ζ) soot-luminosity boundaries or flame-sheet shapes (whichever is appropriate) are illustrated for the same three flames in Fig. 6. First, it is evident that the predictions are in excellent agreement with the measurements for all three flames. Next, the

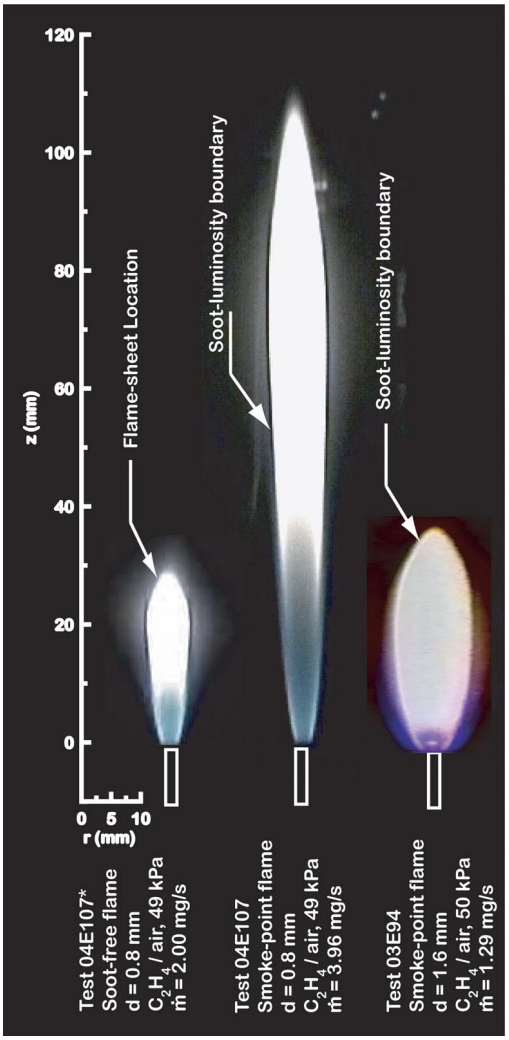

Fig. 5. Photographs of typical flames during the flight experiments illustrating effects of burner fuel flow rate and diameter for ethylene/air flames at 49–50 kPa: left, test 04E107* near the laminar soot point for the 0.8-mm-diameter burner at a fuel flow rate of 2.00 mg/s; middle, test 04E107 near the laminar smoke point for the 0.8-mm-diameter burner at a fuel flow rate of 3.96 mg/s; and right, test 03E94 near the laminar smoke point for the 1.60-mm-diameter burner at a fuel flow rate of 1.29 mg/s.

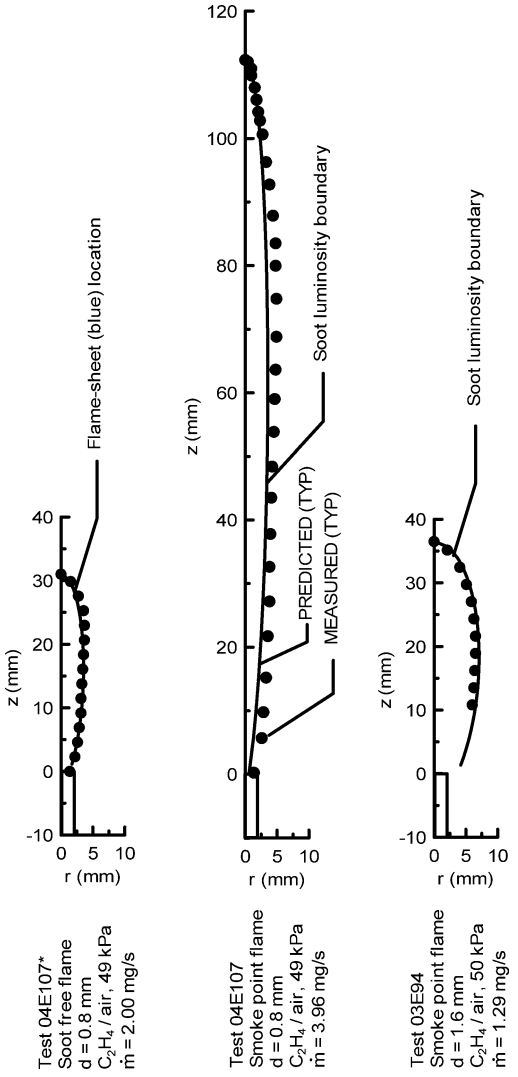

Fig. 6. Measured and predicted flame shapes during the flight experiments illustrating effects of burner fuel flow rate and diameter for the test conditions considered in Fig. 5; predictions based on the extended Spalding [24] approach, Eqs. (6) and (7).

change of soot-luminosity boundaries for the left two flames is caused by the fuel flow rate increase that brings the flame from the laminar soot-point condition to the laminar smoke-point condition. In this case the fuel flow rate nearly doubles, roughly doubling the flame length based on Eq. (3), whereas the empirical flame length parameter, C_f, roughly doubles as well due to spreading of luminous soot particles into the fuel-lean portion of the flame as the flame transitions from laminar soot- to smoke-point conditions. These combined effects explain the roughly fourfold increase in flame length between the left and middle flames in Fig. 6. Finally, the fact that the burner diameter of the right flame is twice the burner diameter of the left two flames explains why the luminous flame diameter of the right flame is twice the luminous flame diameters of the left two flames, through Eq. (4) of the extended Spalding [24] analysis.

Photographs of three flames observed during the flight-based experiments (Fig. 7) show effects of pressure and fuel type on soot-luminosity boundaries at the laminar smoke-point condition for a fixed burner diameter of 0.8 mm. The test parameters of these

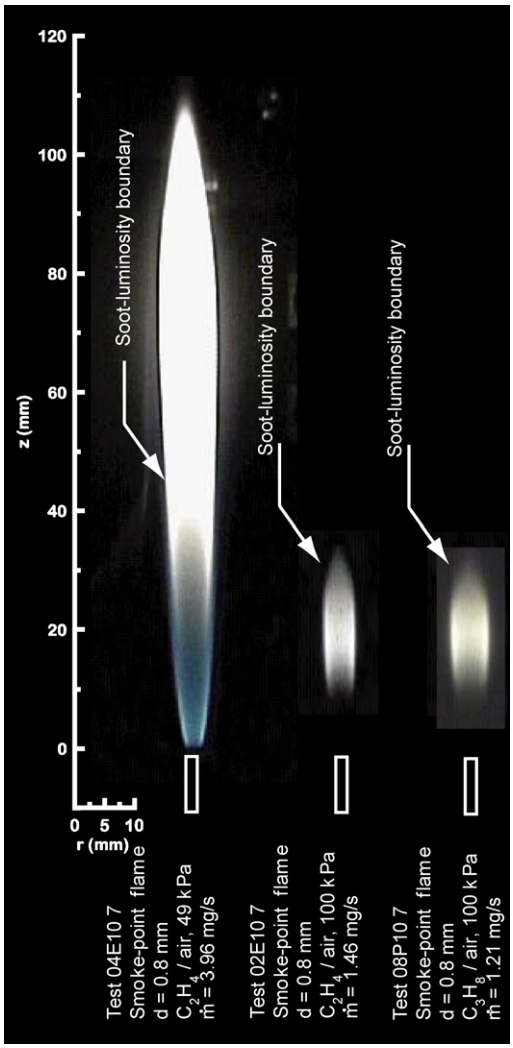

Fig. 7. Photographs of typical flames during the flight experiments illustrating effects of pressure and fuel type for flames using the 0.8-mm-diameter burner; left, test 04E107 for an ethylene/air flame near the laminar smoke point at 49 kPa at a fuel flow rate of 3.96 mg/s; middle, test 02E107 for an ethylene/air flame near the laminar smoke point at 100 kPa at a fuel flow rate of 1.46 mg/s; and right, test 08P107 for a propane/air flame near the laminar smoke point at 100 kPa at a fuel flow rate of 1.21 mg/s.

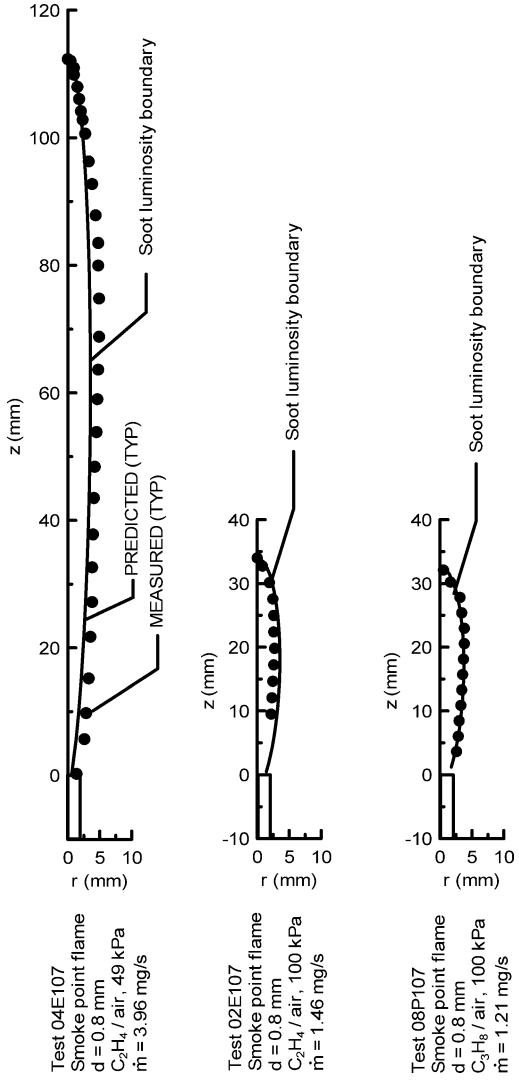

Fig. 8. Measured and predicted flame shapes during the flight experiments illustrating effects of pressure and fuel type for the test conditions considered in Fig. 7; predictions based on the extended Spalding [24] approach, Eqs. (6) and (7).

flames are as follows: the left flame is from test 04E107 for an ethylene-fueled flame at 49 kPa for a fuel flow rate of 3.96 mg/s; the middle flame is from test 02E107 for an ethylene-fueled flame at 100 kPa for a fuel flow rate of 1.46 mg/s; and the right flame is from test 08P107 for a propane-fueled flame at 100 kPa for a fuel flow rate of 1.21 mg/s. Finally, the measured and predicted (with predictions from the extended Spalding [24] analysis) soot-luminosity boundaries are illustrated for the same three flames in Fig. 8. Similar to Fig. 6, it is evident that the predictions are in excellent agreement with the measurements for all three flames. Next, the change in length of the left two flames results because increased pressures decrease the laminar smoke-point flame length for the present flames. The shorter length is reached at the higher pressure, however, because of the reduced fuel flow rates between the left two flames, with negligible effects of pressure on the soot-luminosity flame length which is evident from the results illustrated in Fig. 3. Finally, the stoichiometric mixture fraction, Z_{st}, and the laminar smoke-point flame lengths of ethylene- and propane-fueled flames are not very

different, accounting for the similar soot-luminosity boundaries of the rigth two flames in Figs. 7 and 8.

4.5. Flame shapes (ground-based experiments)

Photographs of three flames observed during the ground-based experiments of Sunderland et al. [20] (Fig. 9) show effects of fuel flow rate, burner diameter, and pressure on the flame-sheet locations of flames burning in air. The test parameters of these flames are as follows: the left flame is from test 16EA for a burner diameter of 0.42 mm with ethane as the fuel at 50 kPa and a fuel flow rate of 0.88 mg/s; the middle flame is from test 01M for a burner diameter of 0.42 mm with methane as the fuel at 98 kPa and a fuel flow rate of 1.70 mg/s; and the right flame is from test 05M for a burner diameter of 0.85 mm with methane as the fuel at 98 kPa and a fuel flow rate of 1.69 mg/s. Finally, the measured and predicted (with predictions from the extended Spalding [24] analysis) flame-sheet locations are illustrated for the same three flames in Fig. 10. First, similar to the results already considered in Figs. 6 and 8, it is evident that predictions are in excellent agreement with the measurements for all three flames. Next, Z_{st} is similar for all the fuels considered during the present study, whereas flame-sheet lengths are not affected significantly as the pressure is changed; therefore, the increase in flame length between the left two flames,

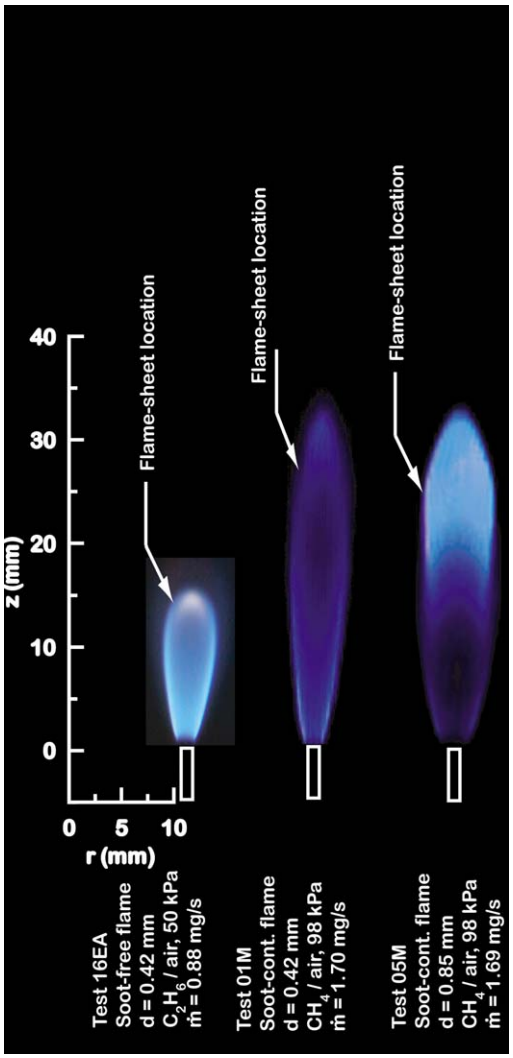

Fig. 9. Photographs of typical flame sheets during the ground-based experiments illustrating effects of burner diameter, fuel type, pressure, and fuel flow rate: left, test 16EA for an ethane/air flame at 50 kPa for the 0.42-mm-diameter burner at a fuel flow rate of 0.88 mg/s; middle, test 01M for a methane/air flame at 98 kPa for the 0.42-mm-diameter burner at a fuel flow rate of 1.70 mg/s; and right, test 05M for a methane/air flame at 98 kPa for the 0.85-mm-diameter burner at a fuel flow rate of 1.69 mg/s.

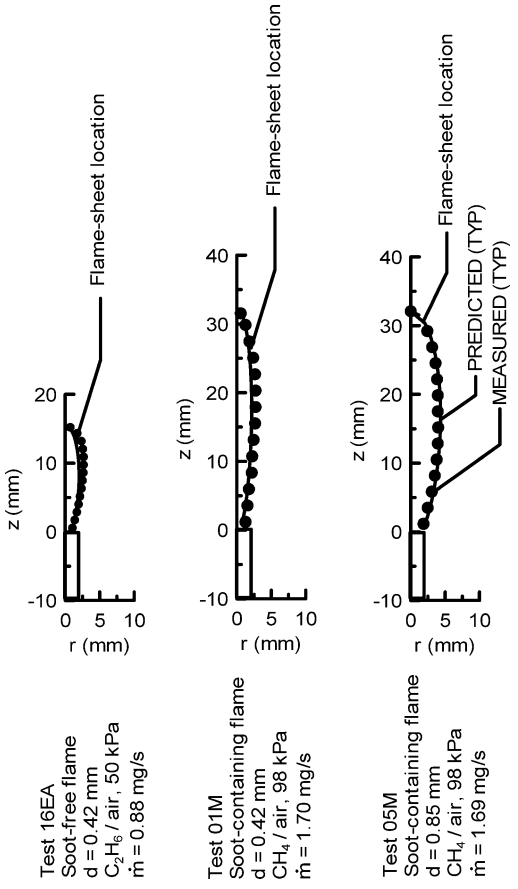

Fig. 10. Measured and predicted flame-sheet locations during ground-based measurements illustrating effects of burner diameter, fuel type, pressure, and fuel flow rate for the conditions considered in Fig. 9; predictions based on the extended Spalding [24] approach, Eqs. (6) and (7).

roughly doubling, is entirely explained by the approximate doubling of the fuel flow rate through Eq. (3). Finally, the right two flames differ only in the burner diameter, which has been doubled from test 01M to test 05M, which doubles the flame-sheet diameter but leaves the flame-sheet length unchanged, as expected from Eqs. (3) and (4).

5. Conclusions

The luminous flame shapes of steady nonbuoyant round laminar-jet diffusion flames in still air were studied using flight- and ground-based microgravity facilities for the experimental observations to avoid buoyant disturbances due to Earth's gravity. Test conditions for the flight-based measurements onboard Space Shuttle Columbia (flights STS-83, STS-94, and STS-107 reported by Urban et al. [4], Lin et al. [5], and the present investigation) were as follows: ethylene- and propane-fueled flames burning in still air at ambient temperatures of 300 K, ambient pressures of 35–130 kPa, jet exit diameters of 0.40–2.70 mm, and jet exit Reynolds numbers of 46–1186 to yield luminous flame lengths of 15–110 mm; with just a few exceptions, these test conditions involved soot-luminosity boundaries (near the laminar smoke-point condition). Test conditions for the ground-based experiments, based on 2.2-s free-fall results reported by Sunderland et al. [20], were as follows: methane-, ethane-, and propane-fueled flames burning in still air at ambient temperatures of 300 K, ambient pressures of 25–48 kPa, jet exit diameters of 0.42–3.25 mm, and jet exit Reynolds numbers of 10–625 to yield luminous flame lengths of 2.5–48 mm; these test conditions involved flame-sheet locations for flames containing various degrees of soot. The combined database was used to evaluate predictions of luminous flame shapes based on the simple classic theory of nonbuoyant round laminar-jet diffusion flames in a still environment of Spalding [24], which was empirically extended to treat effects of the presence of soot in the flames under the laminar smoke-point condition. The major conclusions of the study are as follows:

1. The flames can be classified into groups having closed- and open-tip configurations, with the open tips caused by radiative quenching near the flame tips. Tip opening, however, does not have a strong effect on flame shape properties, except in the vicinity of the flame tip.

2. The simplified analysis of Spalding [24], empirically extended to account for the presence of luminous soot particles beyond the flame sheet near the laminar smoke-point condition, provides excellent correlations of flame-sheet and soot-luminosity boundaries.

3. The luminous length of the flames increases by a factor of roughly two during transition from the flame-sheet boundary to the soot-luminosity boundary at the laminar smoke point, due to the presence of luminous soot particles beyond the flame sheet.

4. For given fuel and oxidant conditions, the flame-sheet length is proportional to the fuel mass flow rate but is independent of the burner diameter; therefore, long and thin (pencil-like) flames can be created using large fuel flow rates and small burner diameters, as long as liftoff and blowout conditions are not exceeded.

5. For given fuel and oxidant conditions, soot-luminosity shapes are qualitatively similar to the properties of flame-sheet shapes discussed in conclusion 3, except that increasing either the fuel flow rate or the pressure tends to increase the luminous flame length due to closer approach of the soot-luminosity boundary to the smoke-point condition with little corresponding effect on the maximum flame diameter.

It should be noted that these conclusions hold for luminous flame lengths over the full range of the measurements; however, the maximum luminous flame-diameter and flame-shape predictions were effective only for sufficiently large flame aspect ratios, i.e., $L_f/d > 10$ or AR > 3.

Acknowledgments

This research was sponsored by NASA Grant NAG3-2404 under the technical management of the NASA Glenn Research Center. The authors acknowledge the contributions of Ann Over and her associates at the NASA Glenn Research Center for development of the test apparatus and the crews of Space Shuttle Columbia flights STS-83, STS-94, and STS-107, who carried out assembly of the test apparatus and performed the experiments on orbit.

References

[1] R.W. Bilger, Prog. Energy Combust. Sci. 1 (1976) 87–108.
[2] S.P. Burke, T.E.W. Schumann, Ind. Eng. Chem. Sci. 20 (1928) 998–1009.
[3] C.K. Law, G.M. Faeth, Prog. Energy Combust. Sci. 20 (1994) 65–113.
[4] D.L. Urban, Z.-G. Yuan, P.B. Sunderland, G.T. Linteris, J.E. Voss, K.-C. Lin, Z. Dai, K. Sun, G.M. Faeth, AIAA J. 36 (1998) 1346–1360.

[5] K.-C. Lin, G.M. Faeth, P.B. Sunderland, D.L. Urban, Z.-G. Yuan, Combust. Flame 116 (1999) 415–431.
[6] P.B. Sunderland, S. Mortazavi, G.M. Faeth, D.L. Urban, Combust. Flame 96 (1994) 97–103.
[7] T.H. Cochran, W.J. Masica, Proc. Combust. Inst. 13 (1970) 821–829.
[8] J.B. Haggard Jr., T.H. Cochran, Combust. Sci. Technol. 5 (1972) 291–298.
[9] R.B. Edelman, O.F. Fortune, G. Weilerstein, T.H. Cochran, J.B. Haggard Jr., Proc. Combust. Inst. 14 (1972) 399–412.
[10] R.B. Edelman, M.Y. Bahadori, Acta Astronaut. 13 (1986) 681–688.
[11] M.Y. Bahadori, R.B. Edelman, D.P. Stocker, S.L. Olson, AIAA J. 28 (1990) 236–244.
[12] M.Y. Bahadori, D.P. Stocker, D.F. Vaughan, L. Zhou, R.B. Edelman, in: F.A. Williams, et al. (Eds.), Modern Developments in Energy, Combustion and Spectroscopy, Pergamon, New York, 1993, Chapter 4.
[13] K.P. Schug, Y. Manheimer-Timnat, P. Yaccarino, I. Glassman, Combust. Sci. Technol. 22 (1980) 235–250.
[14] R.E. Mitchell, A.F. Sarofim, L.A. Clomberg, Combust. Flame 37 (1980) 227–244.
[15] K. Saito, F.A. Williams, A.S. Gordon, Combust. Sci. Technol. 47 (1986) 117–138.
[16] P.B. Sunderland, Ü.Ö. Köylü, G.M. Faeth, Combust. Flame 100 (1995) 310–322.
[17] P.B. Sunderland, G.M. Faeth, Combust. Flame 105 (1996) 132–146.
[18] F. Xu, G.M. Faeth, Combust. Flame 125 (2001) 804–819.
[19] A.M. El-Leathy, F. Xu, C.H. Kim, G.M. Faeth, AIAA J. 41 (2003) 856–865.
[20] P.B. Sunderland, B.J. Mendelson, Z.-G. Yuan, D.L. Urban, Combust. Flame 116 (1999) 376–386.
[21] M. Klajn, A.K. Oppenheim, Proc. Combust. Inst. 19 (1982) 223–235.
[22] S. Mahalingam, J.H. Ferziger, B.J. Cantwell, Combust. Flame 82 (1990) 231–234.
[23] F.G. Roper, Combust. Flame 29 (1977) 219–226.
[24] D.B. Spalding, Combustion and Mass Transfer, Pergamon, New York, 1979, p. 185.
[25] K.K. Kuo, Principles of Combustion, Wiley, New York, 1986, p. 360.
[26] W.G. Braun, R.P. Danner, T.E. Daubert, Technical Data Book—Petroleum Refining, third ed., Am. Petroleum Inst., Washington, DC, 1976, Chapters 11 and 13.